11th International Symposium on Magnetic Bearings
August 26-29, Nara, Japan

PASSIVE MAGNETIC SUSPENSION LIMITATIONS FOR GRAVITY COMPENSATION

J.L.G. Janssen
Dept. of Electrical Eng., Eindhoven University of Technology, The Netherlands
j.l.g.janssen@tue.nl

J.J.H. Paulides
Dept. of Electrical Eng., Eindhoven University of Technology, The Netherlands
j.j.h.paulides@tue.nl

E. Lomonova
Dept. of Electrical Eng., Eindhoven University of Technology, The Netherlands
e.lomonova@tue.nl

ABSTRACT
The development of sophisticated advanced vibration isolation is important, since even the minutest vibrations have disastrous effects on the performance of static and moving parts in high-precision machines. This paper concerns with the isolation of these vibrations for a large static body in an advanced micro-lithographic system, where a passive/active electromagnetic solution is presented. In these configurations passive permanent magnets (PM) provide the gravity compensation and active electromagnets the accurate positioning. However, this paper only considers the applicability of a passive magnetic solution for this high force gravity compensation application, or, more specifically, the influence of various PM array topologies on the force density. Further, fast-solving analytical models will be presented and will consequently be used to illustrate the feasibility of using passive permanent magnets for gravity compensation in this demanding high precision industrial application.

INTRODUCTION
The active anti-vibration application used as a reference in this paper is the advanced micro-lithography machine, referred to as a 'wafer scanner' (Fig. 1a), which is at the heart of integrated circuit (IC) manufacturing. As such, micro-lithography technology has been one of the key enablers and drivers for the semiconductor industry for the past several decades. Improvements in lithography are responsible for roughly half of the improvement in cost per function in IC technology. The underlying reason for the driving force in semiconductor technology has been the ability to keep the cost for printing a silicon wafer roughly constant while dramatically increasing the number of transistors that can be printed per chip. ICs have always been printed optically where improvements in lens and imaging material technology along with decreases in wavelength fuel the steady improvement of the lithography technology.

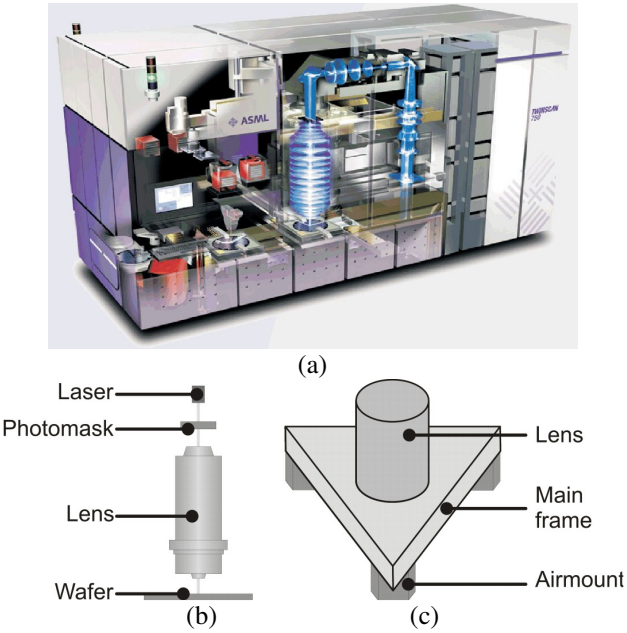

FIGURE 1: (a) Industrial state-of-the-art wafer-scanner of ASML in Eindhoven, the Netherlands, (b) simplified micro-lithography schematic, and (c) simplified schematic of the lens suspension of a wafer scanner [1].

The leading-edge production lithography employs optical projection printing, where the image of the master pattern or mask is projected onto a wafer substrate that has been coated with a photosensitive material. A schematic diagram of an optical lithography system is shown in Fig. 1b. The solubility of the resist is changed by exposure to light so that a pattern emerges upon development (much like a photograph). The remaining resist pattern is then

used for subsequent process steps such as etching or implantation doping. The optical projection systems used today have very complex multi element lenses that correct for virtually all of the common aberrations and operate at the diffraction limit. As such, arguably the most important variable to control is the minimum line width of the circuitry (currently approximately 10s of nanometers).

One of the future bottlenecks in decreasing the line width, and thus circuit density of ICs, is caused by badly damped micro-vibrations of the wafer stepper lens [1]. To date, micro-vibration problems within high-precision machines could often be solved by means of adequate isolation of the equipment from the floor, i.e. the main plate is resiliently isolated from the floor, both passively and actively, by means of three so-called airmounts (Fig. 1c). However, in order to provide an increased bandwidth solution, magnetic mounts could be a possible substitute of the airmount, e.g. in combination with mechanical means [2] or by fully magnetic means [3]. In magnetic mounts two important design criteria exist, namely large force in the *z*-direction and very accurate positioning. This paper focuses on the achievable passive force that can be generated by using only PMs for the *z*-direction. Although that in the final magnetic mount the stability is provided by active means, which is outside the scope of this paper.

The magnetic force calculation requires a careful study of the interaction force between permanent magnets. This is indispensable to obtain a feasible design for the passive gravity compensation, hence magnetic mounts. In order to obtain extremely linear solutions only various combinations of hard magnetic materials in free space are considered in this paper. This does limit the achievable force density, however excludes the non-linearity and hysteresis that would be introduced by the use of soft magnetic materials. The calculation of these forces can be undertaken by various analytical and numerical modeling techniques. In the next section these methods are discussed and subsequently a new rotational technique will be introduced that simplifies the calculation of all the magnetic forces if non-parallel magnetization vectors are apparent in the various permanent magnets.

PERMANENT MAGNET MODELING

In general, 3D finite element modeling of PMs in free space is used to determine the forces, however this is extremely time consuming and therefore an analytical technique will be introduced in this paper that allows calculation of the necessary force components for various magnetization directions.

A range of techniques exist for analyzing PM devices, i.e. charge model and equivalent current model [4]. In this paper, PMs are modeled as distributions of equivalent magnetic charges [5] [6], assuming that no other materials are present that influence the magnetic field, a homogenous and constant (within its volume) magnetization. It needs noting that global deviation of the magnetization vector of the hard magnetic material could be taken into account by using the non-parallel magnetization vector model. A schematic view of two cubical PMs with the respective variables is shown in Fig. 2. Although the magnetic charges and, consequently, the force distribution have no physical meaning, this method is feasible to obtain the global interaction force between PMs [7].

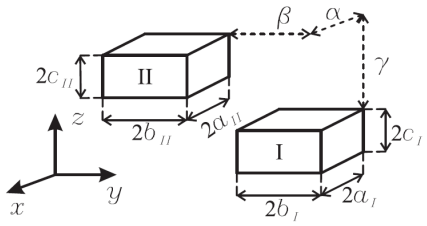

FIGURE 2: Schematic model, showing the respective dimensions and displacement of two permanent magnets.

(Anti-)parallel magnetization vectors

The 3D analytical surface charge method [5], provides analytical expressions of the PM field that are exact for 3D ironless structures, i.e. they are not approximations and, in contrary to the 3D FEM, remain very time inexpensive. More specifically, these analytical solutions are not mesh based, and therefore exhibit their high accuracy especially at large magnetic field gradients (e.g. the magnet edges). In [5] the three cartesian components of the PM magnetic flux density, $\underline{B}$, are derived from the charge model and utilized to obtain the force, $\underline{F}$, between (anti)-parallel magnetized PMs using the virtual work method.

As mentioned, these analytical solutions provide force calculation for (anti-)parallel magnetized PMs, although alternative magnetization vectors, due to either configuration considerations or global misalignment of the magnetization vector, can not be calculated using these formulae. Such alternative magnetization vectors are discussed in [8] with respect to rotating PM couplings, although in this paper rather complicated and non-transparent formulae are utilized. Implementation of a similar method described in [6] learns, that this method of nested functions tends to be slower than the general approach described in [5], which therefore is used in this paper.

Non-parallel magnetization vectors

In this paper a technique is introduced that avoids the complex surface integrals of the vertically oriented field by using a rotational technique to analytically obtain the

force along x, y and z. In this respect, the global force on PM II due to the presence of PM I, as shown in Fig. 2, may be written as [9]

$$\underline{F}_{II} = \oint_S \sigma_m(\underline{r})\underline{B}_I(\underline{r})dS \qquad (1)$$

where S is the surface of PM II, σ_m is the magnetic surface charge density, originating from the surface charge model, and B_I is the magnetic flux density of PM I. Assuming PM I is magnetized along z and PM II along y, the force is obtained by integration over the surfaces in the xz-plane, resulting in

$$F = \frac{B_{r_I} B_{r_{II}}}{4\pi\mu_0} \sum_{i=0}^{1} \cdots \sum_{n=0}^{1} (-1)^{i+\cdots+n} \psi, \qquad (2)$$

where

$$\begin{aligned}\psi_x &= \frac{1}{2}\Bigg[\left(\tan^{-1}\left(\frac{U}{S}\right)+\tan^{-1}\left(\frac{TU}{SR}\right)\right)S^2 + \\ &\quad 2TS - 3US - 2T\log(U+R)\,S - \\ &\quad 2T^2\tan^{-1}\left(\frac{S}{T}\right) + T^2\tan^{-1}\left(\frac{SU}{TR}\right) + \\ &\quad U\left(U\left(\tan^{-1}\left(\frac{S}{U}\right)+\tan^{-1}\left(\frac{ST}{UR}\right)\right) - \right. \\ &\quad \left. 2T\log(S+R) + 2S\log(R-T)\right)\Bigg], \qquad (3)\end{aligned}$$

$$\begin{aligned}\psi_y &= \frac{1}{2}\Bigg[-(S-T)(S+T)\log(U+R) + \\ &\quad 2S\left(T\left(\tan^{-1}\left(\frac{U}{T}\right)+\tan^{-1}\left(\frac{SU}{TR}\right)\right) + \right. \\ &\quad \left. U\log(R-S)\right) + U(R-2S)\Bigg], \qquad (4)\end{aligned}$$

and

$$S = \alpha - (-1)^i a_I + (-1)^l a_{II}, \qquad (5)$$

$$T = \beta - (-1)^j b_I + (-1)^m b_{II}, \qquad (6)$$

$$U = \gamma - (-1)^k c_I + (-1)^n c_{II}, \qquad (7)$$

$$R = \sqrt{S^2+T^2+U^2}. \qquad (8)$$

Due to the formulation of the vertical magnetic flux density [5], ψ_z is complex to derive. Therefore, a rotation technique is applied which enables calculation of F_z in terms of ψ_x and ψ_y as shown in the example in Fig 3. The original coordinate system in Fig 3(a) is rotated to the system shown in Fig. 3(b) which uses (2)-(8) to obtain $F_{x(b)}$ and $F_{y(b)}$. An extra rotation produces the coordinate system in Fig. 3(c), which interchanges PMs I and II, where in this example $F_{x(c)}$ and $F_{y(c)}$ are obtained, from which $-F_{x(b)}$ and $F_{z(b)}$ are derived. Thus, rewriting the obtained forces to the coordinate system (a) will result in the three Cartesian force components.

In the next sections both the (anti-)parallel and non-parallel magnetization vector analytical techniques are used to determine the forces and force densities of various combinations of permanent magnets that could be applicable for the lithography application.

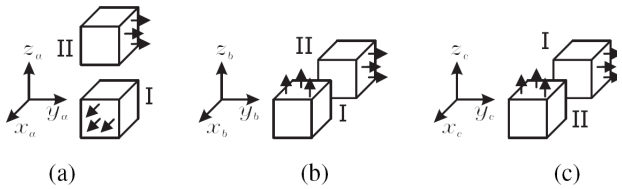

FIGURE 3: Coordinate systems used in the calculation of the interaction force, showing (a) the original coordinate system *a*, (b) transformation in coordinate system *b*, and (c) transformation into coordinate system *c*.

DESIGN CONSIDERATIONS AND ASSUMPTIONS

In the micro-lithography application considered in this paper, the mass of the main plate with equipment is thousands of kilograms. Therefore, a mechanically stiff structure must be considered, i.e. deflection under stress should be minimized and resonance frequencies should be maximized. However, PMs are a ceramic and therefore a brittle material which fails under severe compressive and small tensile stresses. This necessitates a support material to provide the required mechanical stiffness. In this paper, it is assumed that at any time a 10mm thick plate of non-permeable stainless steel needs to be glued to the back of a PM array to provide for sufficient mechanical stiffness. However, off course, for the practical implementation exact analytical or numerical stress calculations are required, which are not considered in this paper.

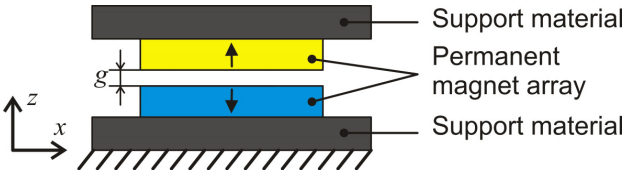

FIGURE 4: Schematic representation of the suspension device and definition of the airgap.

Further, the suspension device has to provide a stable platform, i.e. isolated from external vibrations and minimized influence by forces exerted on the main frame itself. Therefore, the required stroke is limited by the relative displacement between the two bodies. In this paper, the required stroke is defined at 2mm. The minimum airgap, g, is set to 0.5mm, which enables a space to insert the required mechanical (e.g. rubber) end stops, the nominal airgap, schematically shown in Fig. 4, is therefore set at 1.5mm. In the considered application, the outer dimensions of the gravity compensator in the xy-plane are

limited to 100x100mm. This is used to undertake the full parametric search by varying the model parameters such as airgap and vertical dimensions.

To obtain a high force density, hard magnetic materials which have a high remanence are favored. However, the disadvantage of such materials, however, is the slightly higher relative permeability, and reduced intrinsic coercivity. The former leads to a small error in the used analytical model, however, the latter may contribute to demagnetization, hence, irreversible loss. It needs noting that, as shown in (2), the forces scale quadratic with the remanent flux density.

To provide for a practically implemental solution, in this paper the permanent magnet material Vacodym 669 TP is considered, which exhibits a remanent flux density, B_r, of 1.22 T and relative permeability, μ_r , of 1.03. In the analytical calculations the relative permeability is considered to be unity, which has only a minor influence on the force. Further, it is assumed that all PMs operate above their knee-point, which is defined by the intrinsic coercivity. If a part of the material operates below this knee point, partial irreversible demagnetization occurs. This, off course, impairs on the performance of the device and causes the analytical results to be incorrect. Vacodym 699 TP exhibits an intrinsic coercivity of 2230kA/m, or flux density of -1.67T, at the knee point, which ensures that demagnetization is highly improbable. However, to investigate if materials with higher remanence and lower intrinsic coercivity would be feasible, demagnetization is considered in this paper. As such, the magnetic field component along the direction of magnetization inside the PMs is observed for the topologies presented, on a cubical mesh inside the magnet having 0.5mm^3 elements.

In the next sections, a variety of passive suspension topologies will be discussed, starting from a primitive structure. By observing the properties, shape and complexity the topologies are gradually expanded towards bidirectional magnetized topologies and Halbach topologies that exhibit higher force densities. Further, also topologies with multiple airgaps will be investigated.

PRIMITIVE GRAVITY COMPENSATOR

A very primitive form of a gravity compensator would consist of two opposing PMs, as shown in Fig. 5. In this figure, the lower magnet is on the 'fixed' world, hereafter referred to as frame I, where as the upper magnet is connected to the main frame, referred to as frame II.

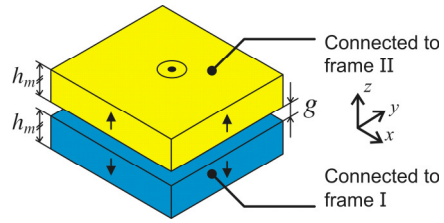

FIGURE 5: Primitive gravity compensator topology composed of two repelling PMs.

The airgap, g, and the magnet height, h_m, are varied to investigate the achievable force levels, as shown in Fig. 6. This demonstrates that the vertical force tends to increase with magnet height and decrease with increasing airgap length.

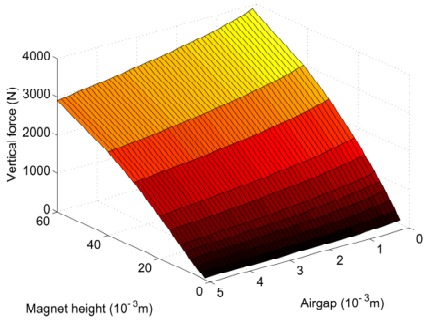

FIGURE 6: Produced force as function of the airgap and the height of the magnet stacks.

As was mentioned, reinforcing materials are necessary for structural support. To be able to compare designs having this reinforcing material, the force density plot takes this additional material into account, shown in Fig. 7. This demonstrates that, for the nominal airgap of 1.5mm, the optimal force density of 2.6N/mm^3 for the unidirectional magnetized topology occurs for a very thick magnet height of 30mm, which corresponds to a force of 3.1kN.

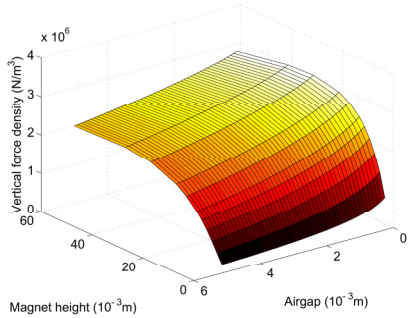

FIGURE 7: Force density as function of the airgap and the height of the magnet stacks.

To investigate the demagnetization the working points of all the various elements ($0.5m^3$) inside both magnets are shown in Fig. 8(a), (each mesh element is represented by a circle). It is visible that all the working points within the magnet are tending towards the zero flux density level, although that a negative magnetic flux density is not observed. This can also be illustrated by the equipotential contours in Fig. 8(b). This also indicates that the flux tubes are not well confined within the structure, and hence, force density is likely to be suboptimal. Several topologies may be applied to reduce such fringing, and to concentrate flux in order to maximize force, of which some are discussed in the next sections.

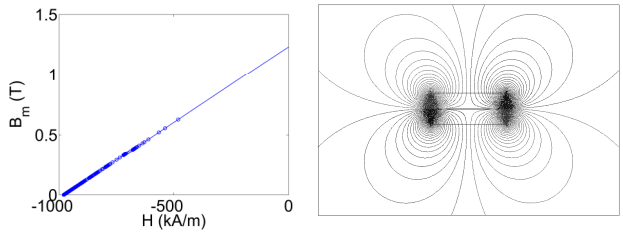

(a) (b)

FIGURE 8: (a) Working points within the PMs and (b) equipotential lines for a homopolar topology having a magnet height of 20mm.

STACKING OF PERMANENT MAGNETS

As magnetic energy is stored in the airgaps between PMs, the hypothesis is that creating multiple airgaps having high flux densities is evident to achieve an increased force density. A stack of PMs glued to two respective frames is schematically shown in Fig. 9(a), where frames I and II have been defined above. The magnetization pattern within this sandwich structure is such, that each PM of frame II is repelled by the magnet below, whilst being attracted by the magnet above. Under load, the interaction force between the PMs is transferred to the frames through the side surfaces of the PMs. This, in combination with the brittle structure of PMs, makes such topology not suitable for the application under focus, as these joints could easily fail by bending.

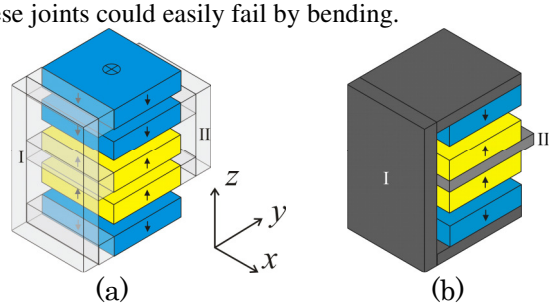

(a) (b)

FIGURE 9: Stacked array of (a) unidirectional permanent magnets with (b) non-permeable steel reinforcement.

To reduce the internal stress, a stacked structure, where the PMs are supported by non-magnetic support material of 10mm thickness, is researched. In this topology, force density is increased by utilizing both sides of the metal to mount PMs, schematically shown in Fig. 9(b), which is composed such, that the sum of the airgaps above and below frame II is 3mm.

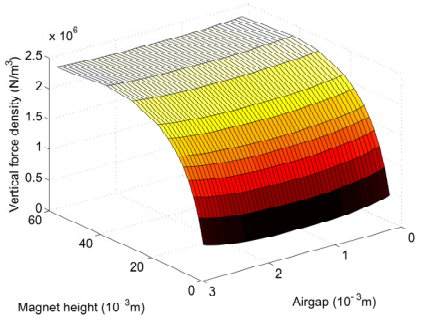

FIGURE 10: Force density as function of the airgap and the height of the magnet stacks.

The force density of the stacked topology is shown in Fig. 10, which displays a clear decrease with respect to the single-airgap configuration. This is caused by the appearance of even more significant fringing and the large areas of opposing magnets, shown in Fig. 11(b). Further, flux in the opposing permanent magnet is reversed, as is also illustrated in Fig. 11(a). Therefore, this topology is not suitable for this application.

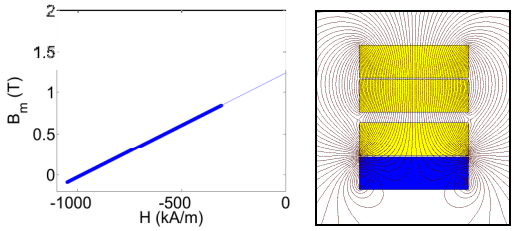

FIGURE 11: (a) Working points and (b) equi-potential contours for the stacked array with reinforcement.

BIDIRECTIONAL MAGNETIZED ARRAYS

The previous topology clearly illustrated that the field around the unidirectional magnetized array are defocused, which highly impairs on the achievable flux density in the airgap, hence, force production. This defocusing can be significantly reduced by bidirectional magnetized arrays, e.g. the 4x4 array of Fig. 12. Due to the periodicity in the topology, a return path for the flux through each PM is provided, hence, an increased force capability.

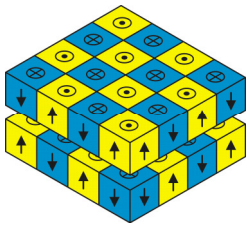

FIGURE 12: Bidirectional magnetized 4 by 4 arrays.

Similar to the unidirectional magnetized topology, the airgap, g, and the magnet height, h_m, are varied. However, an additional variable is the number of segments along the horizontal axes, n, which is varied between 1 and 10, resulting in a n by n array.

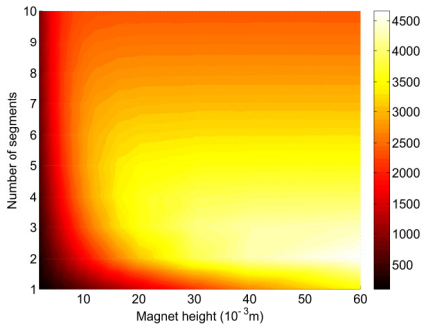

FIGURE 13: Simulated interaction force as function of number of segments and magnet height.

The force computations are shown in Fig. 13 for topologies having an airgap of 1.5mm (nominal airgap). A clear trend can be observed that favors, in terms of force production, low pole numbers with large magnet heights. Therefore, also the force density (Fig. 14) is shown, which clearly demonstrates that the maximum force densities for the bidirectional magnetized array is reached at a relatively low number of segments and small magnet heights, e.g. respectively 5 by 5 with 10mm PMs. For this particular configuration, the corresponding interaction force between the PM arrays is 2.8kN.

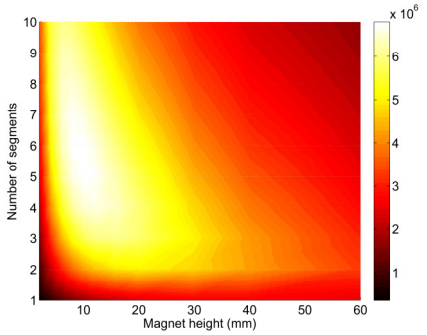

FIGURE 14: Simulated force density for arrays having non-magnetic support structures of 10mm.

The distribution of the PM working points, shown in Fig. 15 for a PM well inside the structure, demonstrates that irreversible demagnetization does not occur in this topology. As such, all field values are positive. Further, the flux tubes plot, shown for a cross-section of the 10 by 10 topology with h_m=10mm in Fig. 16, demonstrates that this particular topology ensures short flux paths, hence, an increased force density. Therefore in the next section multiple bidirectional magnet arrays will be discussed.

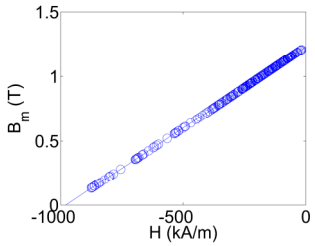

FIGURE 15: Working points inside the middle magnets of the 5x5 array with h_m=10.

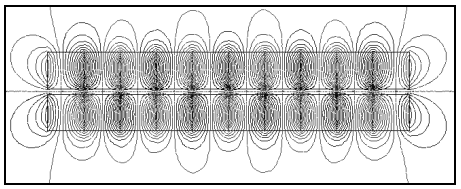

FIGURE 16: Equi-potential contours for the 10 by 10 bidirectional magnetized topology with h_m=10.

BIDIRECTIONAL MAGNETIZED ARRAYS HAVING MULTIPLE AIRGAPS

Fig. 16 illustrated that the flux leakage is very low for the bidirectional magnetized magnet array topology. However, although that the force density is relatively high, the absolute force production is relatively low, respectively 6800 kN/m^3 and 2.8 kN for the 5 by 5 configuration. Hence, in this section the bidirectional magnetized stacked array is considered, schematically shown in Fig. 17.

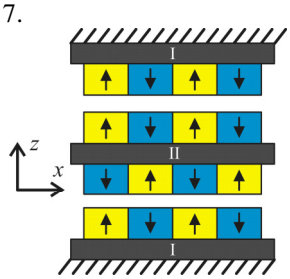

FIGURE 17: Schematic of the stacked bidirectional magnetized array topology.

In this topology, frame II is sandwiched between two arrays of frame I, hence being repelled by the lower array and attracted by the upper array, where the length of the airgaps above and below frame II sum up to 3mm. The resulting interaction force and force density in the middle position are shown in Figs. 18 and 19, respectively. As expected, the maximum force density value has only marginally increased and the optimum is slightly shifted upwards, i.e. towards the 6 by 6 topology having 8mm thick magnet arrays. This particular configuration, off course, provides almost twice the force of the single airgap solution and provides a force and force density of respectively 5.0kN and 7600 kN/m^3.

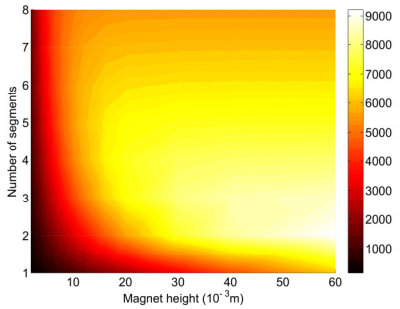

FIGURE 18: Simulated interaction force for the stacked bidirectional magnetized topology.

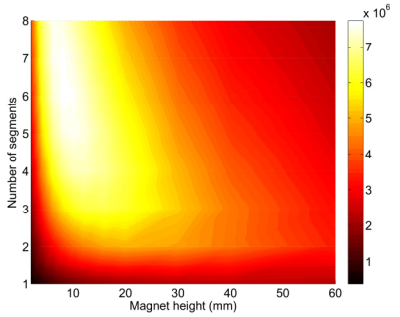

FIGURE 19: Simulated force density for the stacked bidirectional magnetized topology.

This topology clearly showed that flux focusing and flux path length reduction increases both the force density and force capability, hence in the next section an alternative topology is considered that further focuses the permanent magnet array field.

HALBACH ARRAYS

Within permanent magnet array, a well established method to focus magnetic fields is the Halbach array. In this topology, magnets are placed and oriented such, that the magnetic field is focused to one side of the plate, to increases the interaction force between two adjacent PM arrays and to eliminate back-irons. The top view of a Halbach array is shown in Fig. 20 (the resulting field directs out of the paper).

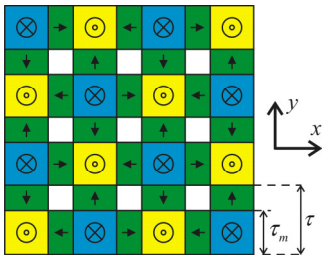

FIGURE 20: 4x4 halbach array illustrating the magnet and pole pitch variable.

With respect to the previously discussed topologies, an extra degree of freedom is observed in the Halbach array, namely the ratio between magnet pitch and pole pitch, or τ_m / τ , as defined in Fig. 20. This optimal ratio depends on the magnet height, however, in this paper, this is not explicitly investigated and therefore fixed to 2/3. The variable n defines the number of vertically oriented PMs along each side of the 100x100mm square magnet plate, where the corner magnets are always vertically oriented.

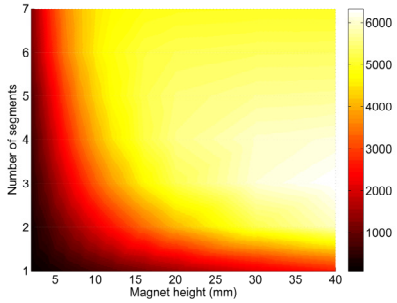

FIGURE 21: Simulated interaction force of the Halbach topology as function of number of segments and magnet height.

Interaction forces are shown in Fig. 21 for Halbach topologies having an airgap of 1.5mm, and, considering the peak force of 6.3 kN, are significantly higher compared to the bidirectional magnetized magnet array topology, albeit at the expense of a significantly larger magnet height, h_m. However, also at a reduced magnet height similar or even increased forces can be achieved, i.e. a 6 by 6 array with a 13 mm magnet height using the multi airgap bidirectional magnetized magnet array of approximately 5.5 kN which is similar to the single airgap Halbach array. However, in the latter topology the total magnet length is 26 mm compared to 52 mm for the multi airgap bidirectional magnetized magnet array topology.

Therefore, investigating this topology in terms of force

density, including the 10mm support structure, Fig. 22 clearly illustrates that very high force densities can be achieved, e.g. using the 6 by 6 or 7 by 7 configuration with a magnet height of respectively 8mm exhibit the highest force density of 11000 kN/m^3.

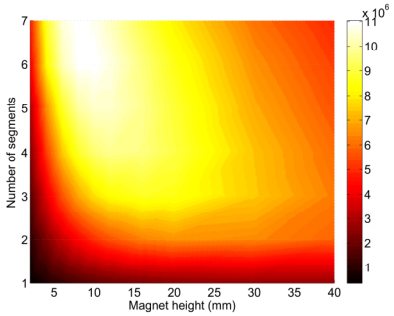

FIGURE 22: Simulated interaction force density of the Halbach topology as function of number of segments and magnet height.

Inherent to the Halbach array is, that adjacent PMs within the array counteract each other, i.e. force each other working points well down the BH characteristic. This is clearly illustrated by Fig. 23(a) and (b), which show the working points for the vertical and horizontal oriented PM, respectively.

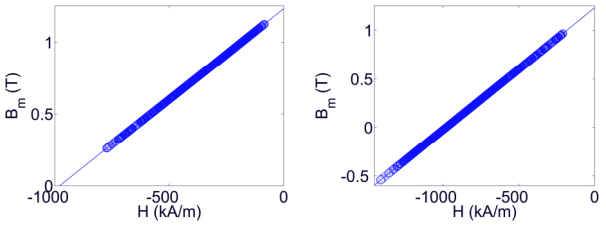

(a) (b)

FIGURE 23: Working points of (a) the vertical magnets and (b) the horizontal magnets.

For the high coercivity permanent magnet considered in this paper this would not provide partial irreversible demagnetization. However, the hard magnetic materials which have a high remanence can not be implemented due to the reduced intrinsic coercivity.

CONCLUSION

This paper demonstrated passive force compensation in vibration isolation systems by PM arrays. Further, using both analytical and finite element methods it is demonstrated that bidirectional magnetized magnets significantly improve the force and force density due to the minimization of the flux leakage and minimizing the flux tubes lengths. In these topologies, the achievable forces are almost linearly proportional to the number of airgaps. On the contrary, the force density is hardly influenced.

As a last topology, a Halbach array is presented, which clearly showed that the lower remanent hard magnetic material is needed to prevent demagnetization. This also provides the highest achievable force density at a relatively high force production, respectively 11000 kN/m^3 and 5.0 kN compared to 7600 kN/m^3 and 5.0 kN for the bidirectionally magnetized arrays. It does need noting that the higher remanent magnets could be implemented in the latter topology, which would increase the force and force density to 10640 kN/m^3 and 7.0 kN, respectively. However, this is achieved at a total magnet length of 40 mm, where the single Halbach array only requires 24 mm. The Halbach will therefore be used to further investigate passive gravity compensation for micro-lithography machines.

REFERENCES

[1] J. Holterman and T.J.A. de Vries, "Active damping based on decoupled collocated control," *IEEE/ASME Trans. on Mechatronics*, vol. 10, no. 2, pp. 135-145, 2005.

[2] T. Mizuno, M. Takasaki, D. Kishita and K. Hirakawa, "Vibration isolation system combining zero-power magnetic suspension with springs," *Control Engineering Practice*, vol. 15, no. 2, pp. 187-196, Feb. 2007.

[3] K. Nagaya and M. Ishikawa, "A Noncontact Permanent Magnet Levitation Table with Electromagnetic Control and Its Vibration Isolation Method Using Direct Disturbance Cancellation Combining Optimal Regulators", *IEEE Trans. Magn.,* vol. 31, no. 1, pp. 885-896, 1995.

[4] L. Medeiros, G. Reyne and G. Meunier, "About the distribution of forces in permanent magnets", *IEEE Trans. Magn.*, vol 35, no. 3, pp. 1215-1218, 1999.

[5] J.P. Yonnet and G. Akoun, "3D analytical calculation of the forces exerted between two cuboidal magnets," *IEEE Trans. Magn*., vol. 20, no. 5, pp. 1962-1964, 1984.

[6] F. Bancel, "Magnetic Nodes", *J. App. Phys*., vol. 32, pp. 2155-2161, 1999.

[7] L. Medeiros, G. Reyne, and G. Meunier, "Comparison of global force calculations on permanent magnets," *IEEE Trans. on Magn.*, vol. 34, no. 5, pp. 3560–3563, Sep. 1998.

[8] J. Charpentier and G. Lemarquand, "Study of permanent-magnet couplings with progressive magnetization using analytical formulation," *IEEE Trans. Magn.*, vol. 35, no. 5, pp. 4206–4217, 1999.

[9] E.P. Furlani, "Formulas for the force and torque of axial couplings", *IEEE Trans. Magn*., vol. 29, no. 5, pp. 2295-2301, 1993.

[10] Cedrat Groupe. [Online]. Available: www.cedrat.com